J. Phys. Chem. A **2003,** *107,* 11139−11152

Can Diarylethene Photochromism Be Explained by a Reaction Path Alone? A CASSCF Study with Model MMVB Dynamics

Martial Boggio-Pasqua,[†,§] Marcella Ravaglia,[†] Michael J. Bearpark,[†,§] Marco Garavelli,[‡] and Michael A. Robb*[,†,§]

Department of Chemistry, King's College, Strand, London WC2R 2LS, U.K., and
Dipartimento di Chimica "G. Ciamician", Università di Bologna, via Selmi 2, 40126 Bologna, Italy

Received: September 25, 2003

The origin of the photochromic properties of diarylethenes is a conical intersection (which we have located computationally), but we show that dynamics calculations are necessary to explain why the conical intersection is accessible, because the excited-state reaction path is not contained in the branching space defining the intersection. Four different systems have been studied: 1,2-di(3-furyl)ethene, 1,2-di(3-thienyl)ethene, 1,2-bis(2-methyl-5-phenyl-3-thienyl)perfluorocyclopentene, and a model hydrocarbon system. Critical points on the ground- and excited-state potential energy surfaces were calculated using complete active space self-consistent field (CASSCF) theory; dynamics calculations were carried out using the molecular mechanics−valence bond (MMVB) method. The main experimental observations (i.e., picosecond time domain, quantum yield, temperature dependence, and fluorescence) can be interpreted on the basis of our results.

Introduction

Photochromism is defined as the reversible phototransformation of a chemical species between two forms having different absorption spectra.[1] A wide variety of materials with potential applications in optoelectronic and photooptical devices[2−5] have been characterized in recent years. Such applications require thermal irreversibility, fatigue resistance, rapid response, high sensitivity, and nondestructive readout capability. Diarylethenes with heterocyclic aryl groups satisfy these requirements, and bisthienylethene-based compounds in particular (X = S, Scheme 1) exhibit remarkable switching sensitivity (i.e. high quantum yield) and rapid response.[5,6]

Recent experimental investigations have focused on the switching dynamics of the ring-closure and ring-opening reactions of photochromic compounds. Time-resolved experimental studies[6−13] have shown that both ring-closure (cyclization) and ring-opening (cycloreversion) reactions in diarylethenes take place in the picosecond time domain and that these rapid transformations do not involve triplet states. The quantum yields for ring-closure can be very high: approaching 1.0 for "edge-to-edge" (antiparallel) conformations, while the "face-to-face" (parallel) conformations are photochemically unreactive.[5,14] Ring-opening quantum yields are generally much lower comparatively (but enhancement of the quantum efficiency can be obtained by means of picosecond laser exposure,[15,16] and it was concluded that a stepwise multiphoton process was the origin of this increased efficiency). The temperature dependence of ring-closure and ring-opening reactions was measured in solution and crystalline phases.[17] Appreciable temperature dependence of the ring-closure rates was not observed, whereas the ring-opening quantum yield increases with temperature. Fluorescence spectra were also measured in a supersonic jet for a compound with thiophene rings bound to the ethene moiety at position 2.[18] The intensity of fluorescence from the open-ring isomer was strong even in solution. The fluorescence intensity modulation by the photoisomerization observed in some diarylethenes[1] and the fact that the dominant species in a supersonic free jet is the "edge-to-edge" (antiparallel) conformer suggest this species is responsible for the emission observed. The dispersed fluorescence spectrum is remarkably red shifted, indicating that the geometry of the molecule changes substantially upon photoexcitation. Fluorescence emission from the closed-ring isomer was also observed recently.[19]

SCHEME 1

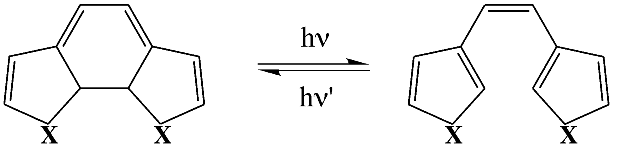

X = O, S

The experimental work described above suggests that there is a delicate balance between adiabatic reactivity (ring-opening and ring-closure) and nonadiabatic processes (yielding ground state products), which can only be rationalized using the potential energy surfaces of the electronic states involved. Older work used semiempirical calculations for some dithienylethene derivatives.[20] Density functional theory (DFT) and time-dependent DFT have also been used.[12,21] Recent, ab initio multiconfigurational self-consistent field (MCSCF) calculations on a model dithienylethene photochromic system were aimed at explaining the stepwise multiphoton process in the ring-opening reaction.[22,23] Our study is focused instead on the behavior of diarylethenes upon one-photon irradiation. We will present a mechanism accounting for the remarkable photochromic properties of diarylethenes, based upon a complete active space self-consistent field (CASSCF) study of the potential energy surface topology and a molecular mechanics−valence

---

* To whom correspondence should be addressed. E-mail: mike.robb@imperial.ac.uk.

[†] King's College.

[‡] Universita di Bologna.

[§] Address beginning January 1, 2004: Department of Chemistry, Imperial College London, South Kensington Campus, London SW7 2AZ, U.K.

10.1021/jp036862e CCC: $25.00

CHART 1

(1)

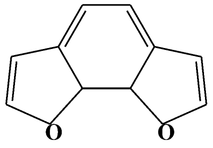

(2)

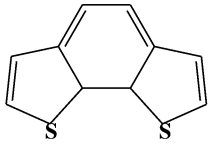

(3)

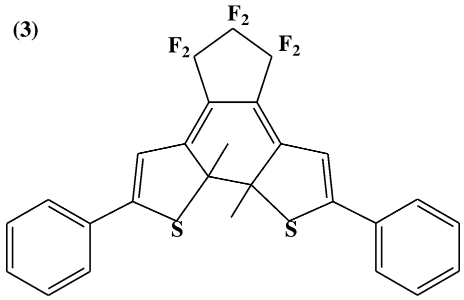

(4)

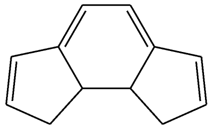

bond (MMVB) computation of the dynamics. Diarylethenes are the first systems we have studied for which dynamics calculations are essential for explaining the observed photochemical behavior qualitatively; a reaction path alone is insufficient.

We studied three diarylethenes (Chart 1) in this work: 1,2-di(3-furyl)ethene (system **1**), 1,2-di(3-thienyl)ethene (system **2**), and 1,2-bis(2-methyl-5-phenyl-3-thienyl)perfluorocyclopentene (system **3**). System **3** is the experimental target system, synthesized and studied in a single-crystalline phase by Irie et al.,[17] whereas systems **1** and **2** are model systems. The dynamics simulations were carried out on the hydrocarbon model system **4**, for technical reasons we discuss in the Computational Methods section.

We cannot fully explain the mechanism of diarylethene photochromism without using some concepts that are relatively new and unfamiliar (or which may be used in an unfamiliar way). We therefore summarize these essential concepts in the next section, before presenting our method and results in detail.

Conceptual Development

The photochromism of diarylethenes and the decay of their first excited singlet states cannot be explained by the topology of the corresponding potential energy surfaces alone. Though we have located a conical intersection between ground and excited states, it is only through dynamics calculations that we can show that such a crossing is accessible: more accessible, in fact, than the transition structure for excited-state ring-closure. As we show below, this follows from the fact that the geometry changes that lift the degeneracy at the crossing (branching space) are quite different from the adiabatic ring-opening/ring-closure coordinate (reaction path). To demonstrate this, we reexamine the prototype conical intersection of $H_3^{\bullet}$ (for a general mathematical discussion, see ref 24), after showing that this situation is analogous to the first excited state of diarylethenes and that the essential ideas will be transferable. Our aim is to contrast two different types of reaction path leading to a surface crossing.

CHART 2

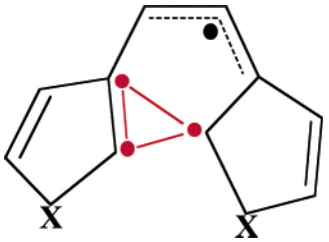

In previous work, we have characterized a general electronic and structural feature of the conical intersections in conjugated hydrocarbons.[25−27] This feature, illustrated in Chart 2 for diarylethenes, was also documented in our previous study of the ring-opening/ring-closure of cyclohexadiene/hexatriene.[28−32] At the conical intersection geometry (Chart 2), one has a triangular arrangement between three unpaired electrons belonging to carbon atoms in the two five-membered rings. These three electrons are weakly coupled π-electrons, and a fourth (belonging to a three-electron allyl fragment) is an uncoupled spectator. Thus, there is a strong electronic and structural analogy with the three-electron conical intersection that occurs in H_3 for all triangular geometries.

$$E^{\pm} = Q \pm \sqrt{K}$$

$$K = (k_{12} - k_{23})^2 + (k_{23} - k_{13})^2 + (k_{13} - k_{12})^2 \qquad (1)$$

The valence bond (VB) expression for the energy of three coupled electrons (viz. H_3) is given in eq 1 above.[33] The exchange integrals k_{ij} are proportional to the overlap between centers i and j, and the variable Q is the Coulomb energy. Clearly, the total exchange K is zero for equilateral triangular geometries ($r_{12} = r_{13} = r_{23}$) in H_3 and the conical intersection is traced out by all such geometries (D_{3h} symmetry), with different energies determined by Q. It is also clear that any nontotally symmetric motion lifts the degeneracy.

The energy of eq 1 is plotted in Figure 1a for two nontotally symmetric motions and in Figure 1b for one totally symmetric motion and one nontotally symmetric motion. In Figure 1a we see the characteristic double-cone structure of an intersection, whereas in Figure 1b the intersection appears as a seam, tracing out equilateral triangular geometries where $K = 0$ and Q varies along q_3. Note that in Figure 1b there is a minimum energy along q_3 at which the two surfaces intersect.

Now let us imagine two possible nonadiabatic reaction paths using Figure 1 as an example. In the first (Figure 1a), we have a reaction path $R_a^* \rightarrow CI(R_a^*/P_a) \rightarrow P_a$ involving only the branching space q_1 and q_2, corresponding to simple downhill decay via the hourglass-like funnel. In the second case (Figure 1b), we not only have a reaction path $R_b \rightarrow CI(R_b/P_b) \rightarrow P_b$ but we also have an orthogonal "valley" ($R'_b \leftrightarrow R''_b$) along a totally symmetric coordinate parallel to the intersection seam q_3. The seam itself can only be accessed via motion perpendicular to the valley, along the nontotally symmetric coordinate q_2. Thus, the accessibility of the nonadiabatic crossing seam in Figure 1b depends on the amount of vibrational energy along coordinate q_2 which is orthogonal to $R'_b \leftrightarrow R''_b$.

In diarylethene molecules, one expects to have a three-electron recoupling scheme at any conical intersection. In Chart 2, one has both π- and σ-electrons being recoupled, leading to

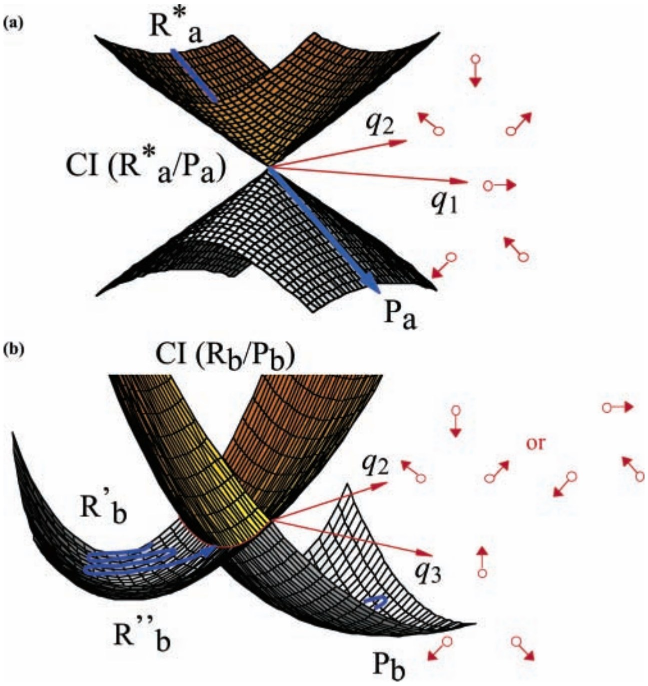

Figure 1. Three-dimensional representation of the S_0/S_1 equilateral crossing in H_3 (a) in the branching space and (b) in a space including a symmetric coordinate q_3 orthogonal to the branching space.

SCHEME 2

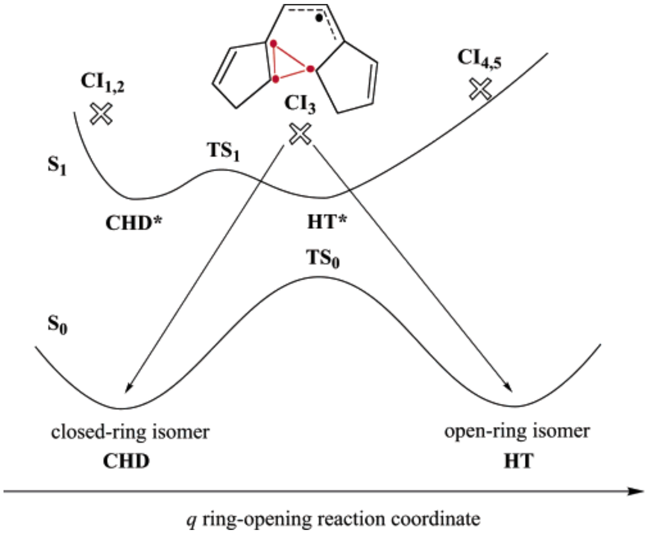

an (approximately) isosceles triangular geometry for the three electrons being recoupled. Nevertheless, eq 1 will still be valid qualitatively, and both types of reactivity embodied in Figure 1 are possible. (Note that this analogy between the excited-state process in diarylethenes and the ground-state process for H_3 is not perfect, as, for example, the latter would not actually pass through the seam but would go around the lower cone of the conical intersection instead.)

Subsequently, we will describe in detail our CASSCF study of the topology of the S_0 and S_1 potential energy surfaces of four different diarylethene molecules, but the results are summarized in Scheme 2.

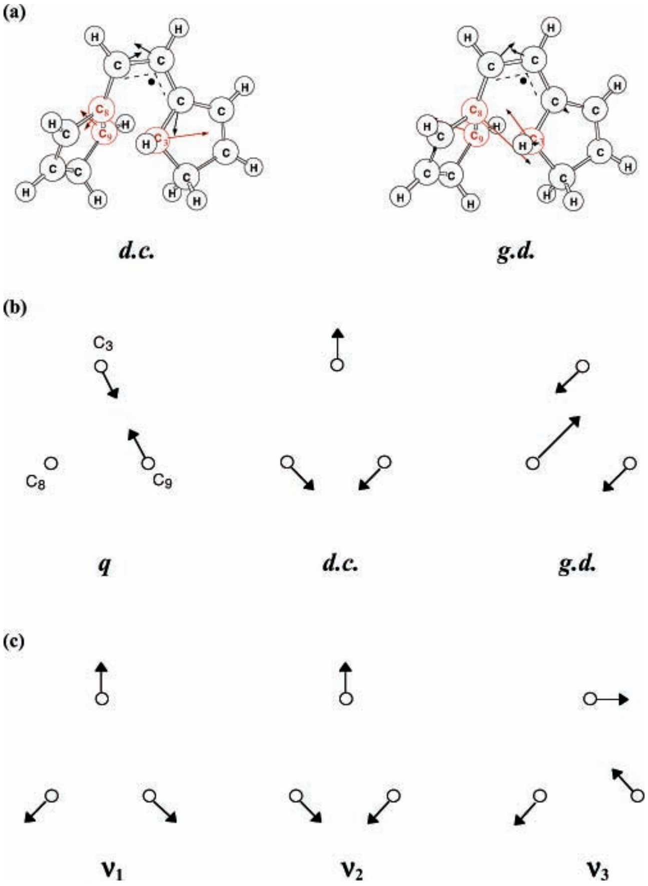

Figure 2. (a) Derivative coupling (*d.c.*) and gradient difference (*g.d.*) vectors at CI_3 in the hydrocarbon model system **4**, (b) the three coordinates to consider in the photochemistry of diarylethenes (*q*: reaction coordinate), and (c) normal modes of vibration for isosceles triangular type molecules (C_{2v} symmetry).

Scheme 2 shows the different critical structures found along the S_1 reaction coordinate *q*. Two minima, a closed-ring isomer (CHD and CHD*, cf. cyclohexadiene) and an open-ring isomer (HT and HT*, cf. hexatriene), were found on S_0 and S_1 for all of the diarylethenes studied. Transition structures (TS_0 and TS_1) were also characterized on each potential energy surface. These results are in general agreement with other ab initio studies by Uchida et al.[22,23] We have also characterized several conical intersection minima (indicated by crosses in Scheme 2) on the closed- and open-ring sides of the potential surface. The conical intersection CI_3 is the most important, because it is the only one that provides a pathway toward both open and closed minima on the ground state. (The other crossings lead back to the corresponding reactant). However, Scheme 2 shows only the reaction coordinate: the conical intersection structures do not lie directly on the reaction path traced by an IRC computation from TS_1 linking CHD* and HT* but should be imagined to be somewhere "behind" the figure, along a parallel coordinate.

In Figure 2a we show the two coordinates that define the branching space[34] of the conical intersection CI_3 (analogous to q_1 and q_2 in Figure 1a). We also show the correspondence between the three coordinates used in Figure 1 for H_3 (Figure 2c) and the coordinates at CI_3 (Figure 2b, extracted from Figure 2a). Because the two coordinates that lift the degeneracy at the crossing CI_3 are orthogonal to the initial reaction path *q* (Figure 2b), CI_3 closely resembles Figure 1b. Thus, the adiabatic S_1 reaction path along *q* (the "valley" in Figure 1b) is not sufficient to understand the photochromism of diarylethenes in detail. Along this path there is competition between the adiabatic S_1 reaction, fluorescence from the CHD* and HT* minima, and radiationless decay to products via, for example, CI_3. This competition must be controlled by the dynamics of the energy flow from the initial reaction coordinate into the orthogonal

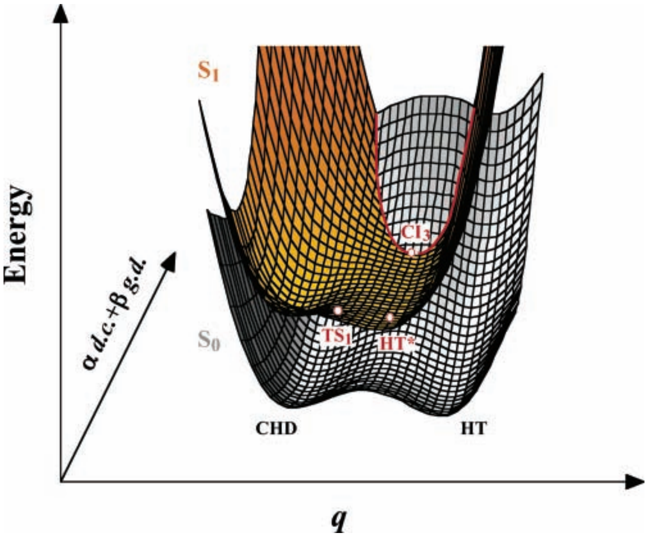

Figure 3. Schematic representation of the structure of the S_0 and S_1 potential energy surfaces corresponding to the closed-ring (CHD) → open-ring (HT) isomerization. The coordinate q is the internuclear distance between the two reactive carbon atoms; *d.c.* and *g.d.* represent the derivative coupling and gradient difference vectors (branching space) which lift the degeneracy at the conical intersection CI_3. The structure TS_1 is the transition state connecting the two excited-state minima CHD* and HT*.

degeneracy-lifting/creating (depending on the direction of motion) coordinates shown in Figure 2a and b.

To understand the energy flow from the reaction coordinate to the conical intersection, we have used MMVB dynamics[35] on a model diarylethene, to demonstrate that the intersection is accessible and to discover the geometries at which nonadiabatic "surface hops" occur. Provided that the topology of the potential energy surfaces is correct (existence of minima, TSs, crossings), the detailed energetics are not vital even in solution: these will affect the time scale of the dynamics simulation but not the mechanistic information we seek. We are also not attempting to compute product quantum yields, and therefore, the description of the crossing region need only be qualitatively correct.

A three-dimensional "cartoon" of the structure of the S_0 and S_1 potential energy surfaces of diarylethenes is presented in Figure 3. This figure is only qualitative but derives from CASSCF calculations of stationary points and the MMVB dynamics simulation. The energy is plotted in a space including one of the degeneracy-lifting coordinates and the S_1 reaction coordinate q (Figure 2b). The reaction coordinate in the photoisomerization of diarylethenes is orthogonal to the branching space associated with CI_3, and the Figure 3 surfaces are topologically similar to those in Figure 1b for H_3: the crossing appears like a seam, parallel to the reaction path (with R'_b = CHD* and R''_b = HT*). However, there is an important difference. In Figure 1b the crossing is peaked,[34] that is, the minima all lie on S_0, while in Figure 3 the crossing is tipped, because corresponding minima on either side of the seam, for example, CHD and CHD*, are on the potential energy surfaces of different states, S_0 and S_1.

Figure 3 can be used to explain the main experimental observations reported above. In our dynamics calculations started from HT*, about 50% of the trajectories decayed (after between 200 fs and 5 ps) at geometries near CI_3, before evolving to the open or closed forms on the ground state. Similarly, trajectories started from TS_1 decayed in the region of CI_3. Thus, CI_3 is *dynamically accessible* from both sides of the S_1 surface: energy can flow from the reaction coordinate q into the coordinates leading to the crossing seam within the time scale of the simulation. The dynamics study supports the suggestion that this crossing seam is involved in both the ring-closure and ring-opening (via TS_1) processes, which is consistent with the very short time scale of these processes. In Figure 3 however, notice that the crossing seam appears on the open-ring side (HT*) of the S_1 surface. Thus, the system has to pass from CHD* through TS_1 to reach the crossing seam CI_3 for ring-opening. This activated process is consistent with the observed temperature dependence of the ring-opening quantum yields[17] and emission from CHD*. Dynamically, passage through a transition state is a "rare" event relative to decay at a potential surface crossing if both have similar energies. Both may be activated as in this case—requiring an energy barrier to be overcome—but the range of accessible crossing geometries is much larger, leading to a larger preexponential factor for decay. Ring-closure is therefore more efficient than ring-opening for the systems represented by Figure 3, because the time required to pass through the transition state TS_1 "bottleneck" for ring-opening is long compared to that for hitting the crossing seam near CI_3 for ring closure. Our dynamics simulations support this, as no trajectory from HT* overcame the transition state TS_1 despite the huge excess of energy available. This is consistent with the lack of appreciable temperature dependence of the ring-closure rates, although our dynamics simulation shows that the system can still remain in the HT* minimum region for up to several picoseconds, which explains the fluorescence observed from the open-ring isomer. Finally, the geometry of the HT* minimum is similar to that of the ground-state transition structure, and the energy gap between the two electronic states considered is much smaller than that in the Franck–Condon (FC) region, both of which are consistent with the fact that the observed dispersed fluorescence spectrum is remarkably red shifted with respect to the excitation energy.

Computational Methods

First, we reemphasize that, in our dynamics simulations, accurate energetics of the potential surface are not vital, but the surface topology (minima, TSs, crossing seams, etc.) needs to be qualitatively correct. Thus, our central objective is to demonstrate that the potential energy surfaces for compounds **1**–**4** in Chart 1 are broadly similar and that the key features of our dynamics simulation for **4** will therefore apply for all four systems. Energy barriers affect the detailed time scales observed in the simulation, but the mechanistic information will still be valid. While the locus of the crossing seam may only be qualitatively correct, this will only affect the accuracy of computed quantum yields. Thus, our objective is to obtain mechanistic information, and we do not attempt to make quantitative predictions.

CASSCF Computations. The most critical decision in CASSCF computations is the choice of the active space (orbitals which can have variable occupancies between 2.0 and 0.0). Due to the large size of the systems under investigation, some compromises have been made concerning the size of the active space and of the basis set. All our calculations used a CAS(10,10) active space consisting of 10 π,π^*-orbitals for the open-ring isomer and 8 π,π^*- plus 2 σ,σ^*-orbitals (describing the sigma bond which is made/broken) for the closed-ring isomer. Exploratory calculations including the lone pairs of the heteroatoms in the active space did not lead to significant differences for the lowest energy structures,[23] and the excited states under consideration do not involve excitations from any lone pair electrons. Basis sets[36] ranging from STO-3G to 6-31G* were used, depending on the system. Time-dependent density functional theory (TDDFT; B3LYP functional with the standard 6-31+G* basis) was used to compute oscillator strengths at Franck−Condon (FC) geometries. All calculations were performed with a development version of *Gaussian 99*.[37]

Stationary points were optimized at the CASSCF level without any symmetry constraints (unlike previous calculations[22,23]). Numerical frequency calculations were used in all of our computations to determine the nature of the stationary points. Conical intersections were optimized using the algorithm described in ref 38. To obtain a very accurate gradient in this procedure, one should compute the orbital rotation derivatives via state-averaged coupled-perturbed MCSCF theory.[39] This is a very expensive procedure, and these (usually small) corrections have been neglected here.

Full investigation of the potential surface topology (intrinsic reaction coordinates, initial reaction direction, and frequency calculations) was carried out for system **1** only, as the calculations are less expensive for that system. We used a modest 4-31G basis set, as this is sufficient to provide qualitative information on the potential energy surfaces. The effect of including polarization functions was assessed for system **2**. A minimal STO-3G basis set was used for system **3** because of the computational demands. Intrinsic reaction coordinates (IRCs) were calculated from all transition structures. Reaction paths on S_0 leading down from the conical intersection were calculated using the constrained optimization algorithm described in refs 31 and 40. This “initial reaction direction” (IRD) search for steepest descent directions from a singularity enables reaction paths to be located without having to compute force constants, starting at points on a potential energy surface where the gradient is not zero. The same IRD method was also used to locate reaction paths from the vertically excited open-ring and closed-ring isomers on the S_1 state.

MMVB Dynamics. The MMVB hybrid method[41] uses the molecular mechanics MM2 force field[42] to describe an inert molecular σ-framework and a parametrized Heisenberg Hamiltonian[43] to simulate CASSCF active orbitals in a valence bond space. Because of the nature of the Heisenberg Hamiltonian, MMVB only has the capability to reproduce CASSCF potential energy surfaces for covalent electronic states at present. MMVB has already been tested for 10 active electrons systems, reproducing CASSCF geometries for the S_0 and S_1 states of naphthalene[44] and azulene.[45] However, VB parameters are currently available for sp^2 and sp^3 carbon atoms only, limiting the treatment of electronic excitation and bond making/breaking to these centers. This is the reason MMVB calculations had to be performed on a hydrocarbon model system (system **4**, Chart 1). Nevertheless, as we show later, **4** has the same potential energy surface topology as **1**, **2**, and **3** (Chart 1).

MMVB can describe the formation of new σ-bonds from p-orbitals in a π-system. However, we encountered some problems here with our current parametrization of the terms in the Heisenberg Hamiltonian needed to describe this new bond formation, specifically, the behavior of the formulas for determining Q_{ij} at long range (>2.5 Å).[41] To try to minimize the problem, we included only the Q_{ij} terms necessary to describe the formation of the one new σ-bond (Scheme 1). However, CHD structures (with the new σ-bond) are consequently much too low in energy relative to HT structures on a particular potential energy surface.

The MMVB energy and gradient are used to solve the Newtonian equations of motion for diarylethenes.[46] Full details of our implementation have been given elsewhere.[35] This is a “direct” dynamics method: the trajectories are propagated using a series of local quadratic approximations to the MMVB potential energy surface, as suggested by Helgaker et al.[47] The step size is determined by a trust radius. The surface-hopping algorithm of Tully and Preston[46] is used to allow excited-state trajectories to transfer to the ground state in the conical intersection region, where strong nonadiabatic coupling effects appear. The difference in energy between S_0 and S_1 at the hop is then redistributed along the component of the momentum parallel to the nonadiabatic coupling vector to ensure total energy conservation.

TABLE 1: CASSCF(10,10)/4-31G Energies[a] for System 1 at Optimized Geometries

geometry	$\Delta E(S_1-S_0)$	$\Delta E(S_0)$	$\Delta E(S_1)$
HT	148.7	0.0	57.6
HT*	35.2	56.0	0.0
CI_1	<0.1	114	23
CI_2	<0.1	129	38
CI_3	0.1	124	33
CI_4	0.6	131	41
CI_5	<0.1	139	48
CHD	116.0	3.8	28.7
CHD*	60.1	27.0	−4.0
TS_0	38.8	53.9	1.6
TS_1	49.3	47.1	5.2
C_2-HT*	38.5	53.2	0.5

[a] Energies are in kilocalories per mole. Energies at conical intersection geometries are state-averaged. $\Delta E(S_0)$ and $\Delta E(S_1)$ are calculated with the open-ring S_0 and S_1 minimum energies, respectively, as references.

On the HT side, initial conditions (geometries and velocities) were obtained from a ground-state trajectory, sampled after 1 ps, where the total energy was reduced compared to the zero-point vibrational energy and two dihedral angles were constrained to forbid the free rotation of the five-membered rings around the σ-bonds. This avoids the system flipping between various open-ring conformers from which ring-closure cannot proceed. We believe that this is a realistic simulation of the experimental conditions when a single crystal is irradiated or when a diarylethene is spatially confined to increase the population of the photoreactive (switchable) antiparallel conformer.

Trajectories starting from TS_1 were sampled directly on the S_1 potential energy surface. The phase of the transition vector was chosen such that ring-opening occurred.

All trajectories were run for a few picoseconds.

Results and Discussion

CASSCF Computations for Molecules 1, 2, and 3. The CASSCF ab initio results for systems **1**, **2**, and **3** are collected in Tables 1−5. A qualitative energy profile along the reaction coordinate, as well as the positions of five conical intersections, is given in Scheme 2. The optimized structures found for system **1** (Chart 1) are presented in Figures 4−6, while the structures for systems **2** and **3** are available as Supporting Information (Figures S1−S5).

For the ring-opening/ring-closure reactions of diarylethenes, the two lowest electronic excited states are the 1B and 2A states in the Franck−Condon region. The 1B state is dominated by the single excitation from the HOMO to the LUMO ($\pi \rightarrow \pi^*$) and presents a strong ionic character. This state is the optically active state, whereas the covalent 2A state is a dark state, as shown by our TDDFT calculations: the oscillator strength was computed to be 0.18 (CHD geometry) and 0.09 (HT geometry) for 1B and 0.01 for 2A (at both geometries). The most accurate

TABLE 2: CASSCF(10,10)/6-31G Energies[a] for System 2 at Optimized Geometries

geometry	$\Delta E(S_1-S_0)$	$\Delta E(S_0)$	$\Delta E(S_1)$
HT	144.3	0.0	56.1
HT*			0.0
CI_2	<0.1	113.0	~25
CI_3	<0.1	122.0	~33
CHD	110.0	−1.0	21.0
CHD*			−8.3
TS_0		50.3	
TS_1			5.9

[a] Energies are in kilocalories per mole. Energies at conical intersection geometries are state-averaged. $\Delta E(S_0)$ and $\Delta E(S_1)$ are calculated with the open-ring S_0 and S_1 minimum energies, respectively, as references.

TABLE 3: CASSCF(10,10)/6-31G* Energies[a] for System 2 at Optimized Geometries

geometry	$\Delta E(S_1-S_0)$	$\Delta E(S_0)$	$\Delta E(S_1)$
HT	144.0	0.0	54.2
HT*			0.0
CI_2	<0.1	112.0	~22
CI_3	<0.1	118.0	~28
CHD	112.0	3.3	26.0
CHD*			−5.2
TS_0		53.8	
TS_1			6.0

[a] Energies are in kilocalories per mole. Energies at conical intersection geometries are state-averaged. $\Delta E(S_0)$ and $\Delta E(S_1)$ are calculated with the open-ring S_0 and S_1 minimum energies, respectively, as references.

TABLE 4: CASSCF(10,10)/STO-3G Energies[a] for System 3 at Optimized Geometries

geometry	$\Delta E(S_1-S_0)$	$\Delta E(S_0)$	$\Delta E(S_1)$
HT	159.8	0.0	57.9
HT*			0.0
CI_3	<0.1	119.0	19.3
CHD	120.6	−0.5	18.2
CHD*			−23.2
TS_0	61.8	54.4	14.3
TS_1			2.3

[a] Energies are in kilocalories per mole. Energies at conical intersection geometries are state-averaged. $\Delta E(S_0)$ and $\Delta E(S_1)$ are calculated with the open-ring S_0 and S_1 minimum energies, respectively, as references.

TABLE 5: CASSCF(10,10)/4-31G Energies[a] for System 3 at Optimized Geometries

geometry	$\Delta E(S_0)$	$\Delta E(S_1)$
HT	0.0	
HT*		0.0
CHD	5.5	
CHD*		−11.4

[a] Energies are in kilocalories per mole[1]. $\Delta E(S_0)$ and $\Delta E(S_1)$ are calculated with the open-ring S_0 and S_1 minimum energies, respectively, as references.

computations on hexatrienes[48] show that the 2A/1B states are degenerate in the Franck−Condon region. As a consequence, the initially excited 1B state decays within a few femtoseconds to the 2A state.[49] The experiments of Fuss show that, in the photoexcitation of the B state of cyclohexadiene, the A state is populated within 10 fs.[50] Because there is a close similarity between the electronic structures of the excited states of diarylethene derivatives and the systems mentioned above, we expect that internal conversion from the 1B state to the 2A state will be rapid in diarylethenes too. Moreover, it seems reasonable that the 2A state is below the 1B state as it is in octatetraene, the chromophore in the closed-ring form of the diarylethenes. CASPT2 and MRMP calculations[51,52] on *all-trans*-octatetraene show the $1B_u$ ionic state is just 0.04 and 0.19 eV, respectively, above the $2A_g$ covalent state. We can therefore assume that these two states are close in energy in diarylethenes as well and that rapid radiationless decay from 1B to 2A occurs in the Franck−Condon region soon after initial irradiation. Thus, in this section we shall concentrate on the behavior of the covalent A state potential energy surface, since it is well established that the photochemical transformations occur on this surface.

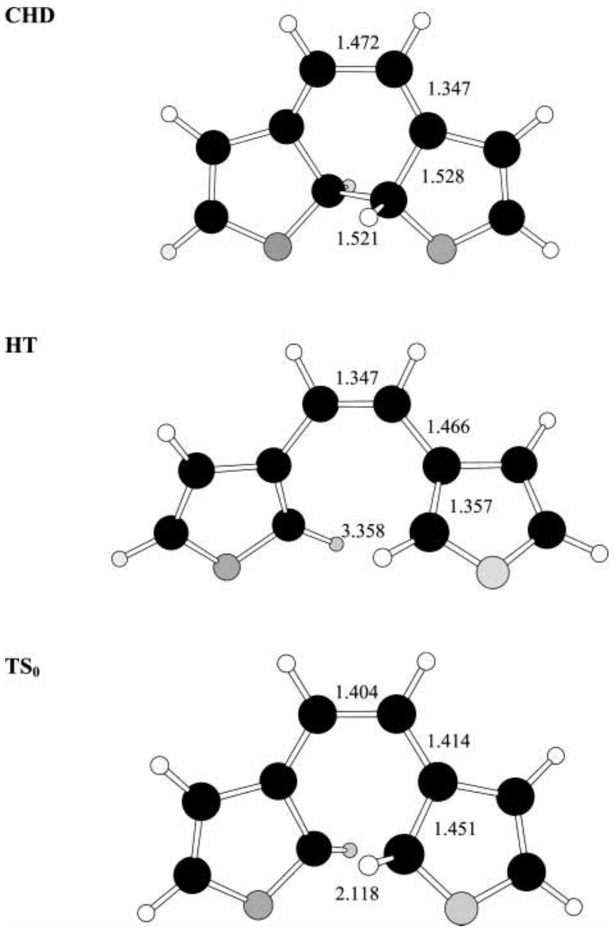

Figure 4. Optimized structures on the S_0 potential energy surface of system **1** at the CASSCF(10,10)/4-31G level. Distances are in angstroms.

For the ground-state S_0, two minima (corresponding to open- and closed-ring isomers denoted HT and CHD, respectively, because of their resemblance to hexatriene and cyclohexadiene) and a transition structure connecting them (TS_0, Scheme 2) were located on the potential energy surfaces of systems **1**−**3**. All these structures have C_2 symmetry, as shown in Figures 4, S1, and S3, in agreement with the calculations of Guillaumont et al.[23] The reaction coordinate leading to the HT product involves a simultaneous σ-bond breaking and complete reorganization of the π-electronic system. The closed-ring form is found to be less stable by a few kilocalories per mole, but this order depends on the basis set used, as shown in Tables 1−5. Considering the limited accuracy of the calculations and the small differences in energy between the two isomers, we cannot say for certain which isomer—CHD or HT—is lower in energy. A large potential energy barrier (~50 kcal mol^{-1}) connecting these two minima was found for systems **1**−**3**, accounting for the thermal stability of both isomers.

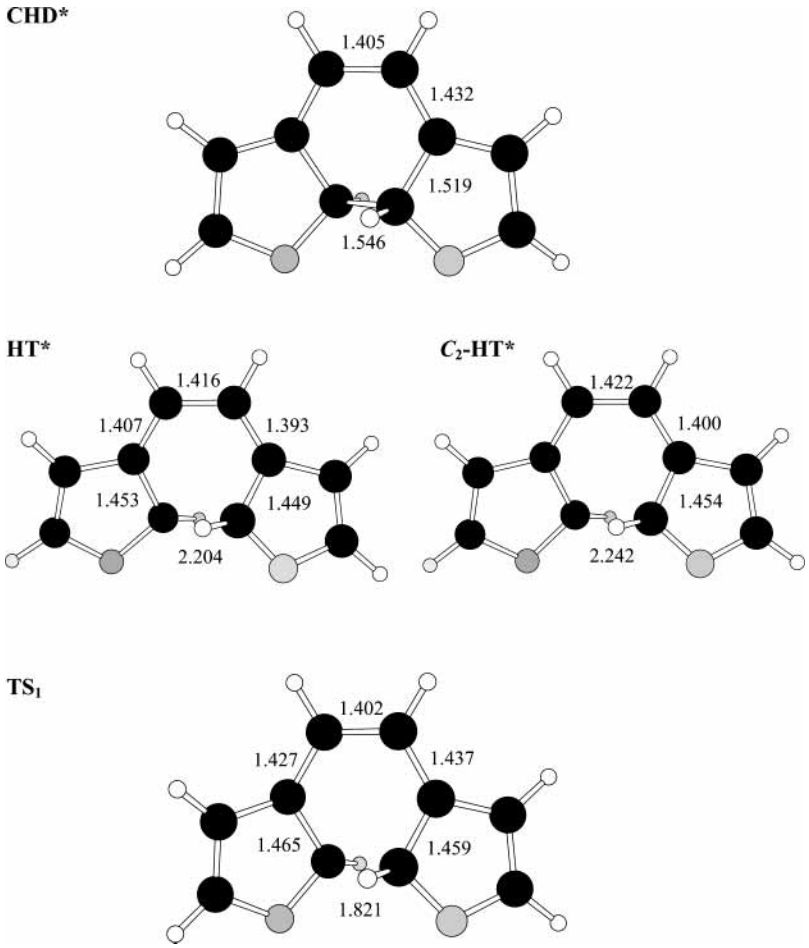

Figure 5. Optimized structures on the S_1 potential energy surface of system **1** at the CASSCF(10,10)/4-31G level. Distances are in angstroms.

On the S_1 excited state a C_2 minimum was located, corresponding to the closed-ring form (CHD*, Scheme 2) for systems **1**−**3** (see Figures 5, S2, and S4). A C_2 stationary point was also found for the open-ring form HT*, but a frequency calculation at this geometry for system **1** reveals a negative direction of curvature along a mode that breaks the C_2 symmetry. This transition structure (labeled C_2-HT*) connects two equivalent asymmetric minima (HT*, Figure 5), which are located at the bottom of a very flat double well (with the barrier to interconversion of only 0.5 kcal mol^{-1} for system **1**). On the other hand, the HT* minimum is found to have C_2 symmetry for system **2**, in agreement with the results of Guillaumont et al.[23] A similar topology to that of system **1** has already been found in the case of the cyclohexadiene/hexatriene system.[29] This is not surprising, as the part of the molecular framework involved in the electronic reorganization is of the hexatriene type. This flat double well may disappear, depending on the level of theory and the substituents or heteroatoms involved.

The closed-ring isomer CHD* was found to be the more stable of the excited-state minima, which is the reverse of the order found for the ground state. CHD* was computed to be just a few kilocalories per mole more stable than HT* for systems **1** and **2** (Tables 1 and 2). The asymmetric transition state TS_1 (Figure 5) that connects CHD* and HT* was located less than 10 kcal mol^{-1} above CHD* in system **1**. Thus, the energy barrier along the reaction coordinate from the closed-ring minimum to the open-ring minimum decreases on going from the S_0 surface (∼50 kcal mol^{-1}) to the S_1 surface (∼10 kcal mol^{-1}). It is worth noting that the TS_1 barrier does not exist in the cyclohexadiene/hexatriene system. As the excited-state conrotatory reaction is allowed according to the Woodward−Hoffmann rule based on π-orbital symmetries for hexa-1,3,5-triene,[53] the diarylethene barrier is probably due to steric constraints from the sigma framework.

Five S_0/S_1 conical intersections were found for system **1** at energies accessible from the Franck−Condon regions (see Figure 6 and Table 1). Two conical intersections (CI_1 and CI_2) are located on the closed-ring isomer side ($q < 1.6$ Å, where q is the distance between the two reactive carbon atoms), whereas two (CI_4 and CI_5) are on the open-ring side ($q > 3$ Å). The central CI (CI_3) is located at an intermediate geometry region ($q = 2.05$ Å) and is similar to the conical intersection found in *cZc*-hexatriene.[28,32] Only CI_1 appears to have a near-C_2 structure, with all the other CIs being asymmetric. As discussed in the Conceptual Development, CI_1 through CI_5 belong to a well-known class of conical intersections involving an unusual out-of-plane distortion, a “kink” of a segment of the polyene chain.[25−27] This type of CI is associated with three weakly coupled π-electrons and a fourth spectator. The “kink” is located in the central CC bond in the case of CI_1 and CI_4, whereas it is found in the furyl rings for CI_2 and CI_5. The CI_3 structure involves an inter-ring “kink”, since the triangular shape occurs between one carbon atom belonging to a furyl ring and two others of the other ring.

Reaction paths on S_0 from the conical intersections were calculated using the IRD procedure described in the Computational Methods section. Direct relaxation on S_0 from CI_1 and CI_2 leads only to the formation of CHD, whereas relaxation from CI_4 and CI_5 leads to HT. However, relaxation from CI_3 can lead to either CHD or HT, as two reaction pathways develop

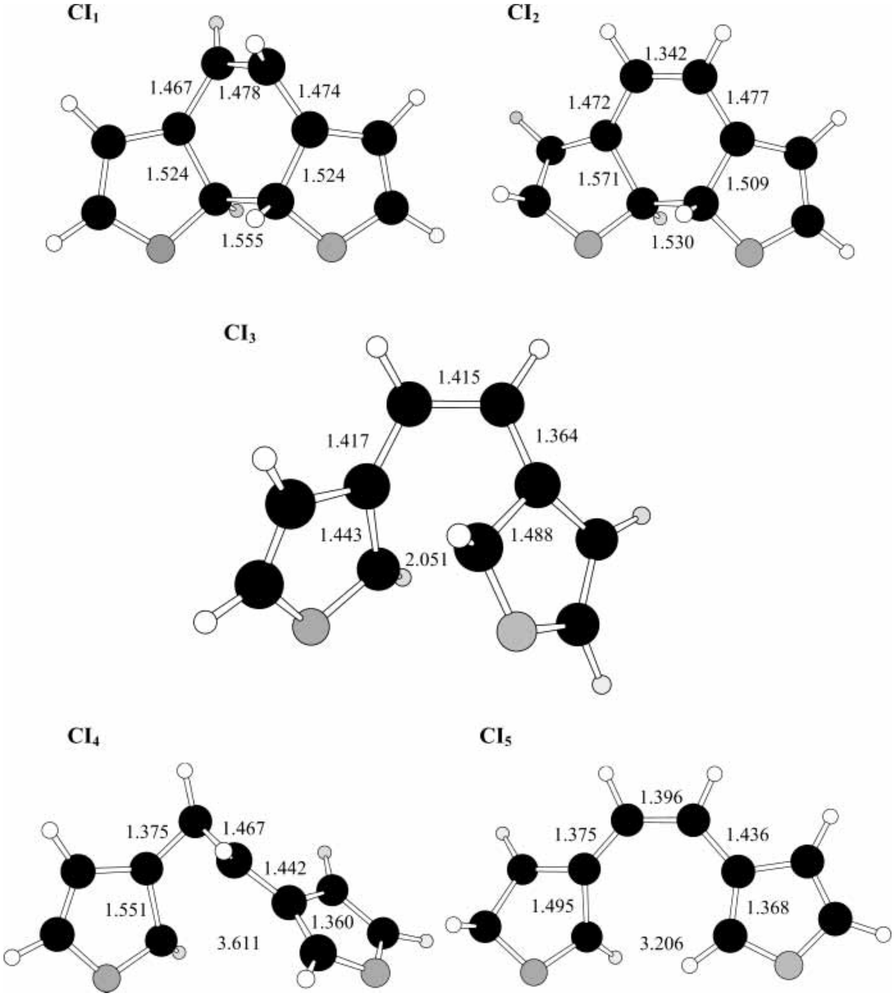

Figure 6. Optimized S_0/S_1 conical intersections at the CASSCF(10,10)/4-31G level in system **1**: closed-ring CI_1, closed-ring CI_2, intermediate CI_3, open-ring CI_4, and open-ring CI_5. Distances are in angstroms.

from CI_3 (Figure S6). It is likely that many other CIs exist in this kind of system, but we believe the five structures discussed here are the most important ones. (For example, two other higher-energy crossing geometries are presented in the Supporting Information, Figure S7.)

CI_1 through CI_5 are all located more than 20 kcal mol^{-1} (Table 1) above the S_1 minima (33 kcal mol^{-1} for CI_3). However, these CASSCF energies have not been corrected for dynamic electron correlation. The CI in hexatriene is 18 kcal mol^{-1} above the excited *cZc*-hexatriene minimum at the CASSCF level, but one estimate using dynamic correlation gives a crossing point lying only 1.0 kcal mol^{-1} above the excited *cZc*-hexatriene minimum.[28] Thus, the CI structures may be stabilized when dynamic electron correlation is accounted for. Nonetheless, one can have confidence that the topology of the surface is qualitatively correct at the CASSCF level. Moreover, CI_3 is suspected to be involved in the photochromism of diarylethenes, as it is the only crossing that offers distinct reaction pathways to both open and closed photoproducts. (Our dynamics simulation—details below—further supports this.)

To ensure that the topology of the potential energy surfaces is conserved between the different systems (Chart 1), we have optimized conical intersection CI_3 for systems **2** and **3**. Figure S5 shows that the resulting structures are very similar to the one optimized for system **1** (Figure 6), and this reassures us that system **1** is a good model system for this study. We would expect to find similar CIs to $CI_{1,2,4,5}$ in systems **2** and **3** as well.

The ring-opening reaction follows irradiation of CHD. Initially, the system evolves on the 2A potential energy surface to reach the S_1 closed-ring minimum CHD* via relaxation of the π-system (Figures 4 and 5). Subsequently, the system can cross the barrier TS_1 (9 kcal mol^{-1}) to reach the flat HT* plateau, provided there is sufficient energy in the ring-opening coordinate which dominates CHD* (1.546 Å) → TS_1 (1.821 Å, Figure 5). This is similar to motion in the valley discussed in connection with Figure 1b in the Conceptual Development section, and as in Figure 1b, the relaxation funnel (conical intersection CI_3) can be reached via vibrations orthogonal to the initial motion in the valley. Decay at CI_3 leads toward HT on S_0.

In the ring-closure reaction an IRD from the FC geometry on S_1 leads to the transition structure C_2-HT*. The resulting path bifurcates toward one of the two equivalent asymmetric HT* minima. The CI_3 funnel can then be accessed, again via vibrations orthogonal to the reaction path, leading to the formation of CHD on the S_0 potential energy surface.

The key difference between ring-opening and ring-closure reactions is that the CI_3 crossing is on the HT "side" of the TS_1 barrier (Figure 3). From either CHD* or HT*, it will take a finite time for sufficient energy to flow into the coordinate leading from the minimum to TS_1. However, from HT*, there is a greater chance of encountering the crossing CI_3 first, as the crossing extends over a wide range of geometries. In other words, the transition state looks like a small "bottleneck"

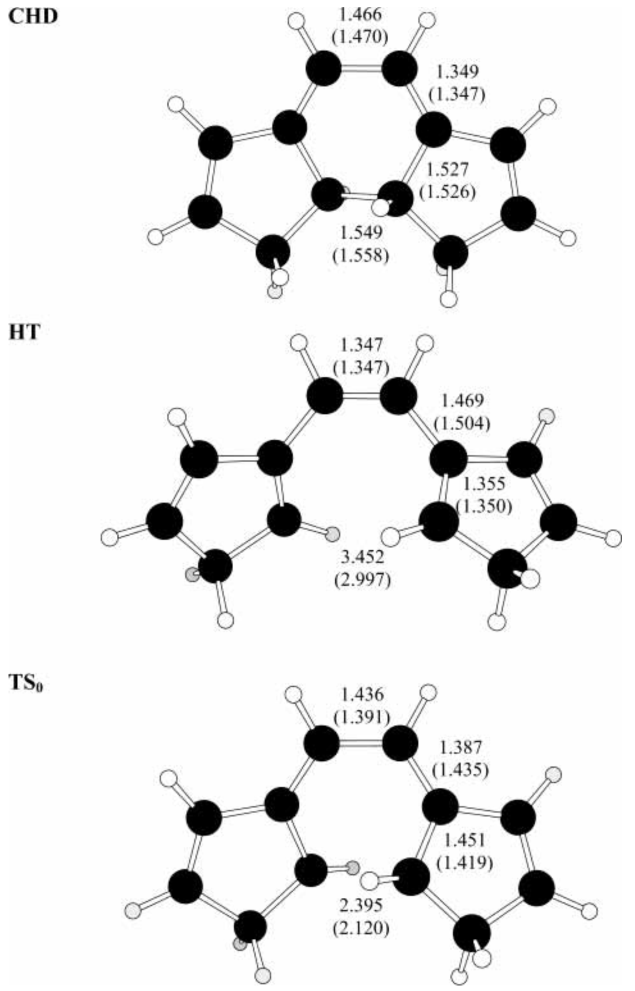

Figure 7. Optimized structures on the S_0 potential energy surface of system **4** at the CASSCF and MMVB levels. MMVB distances are in parentheses. Distances are in angstroms.

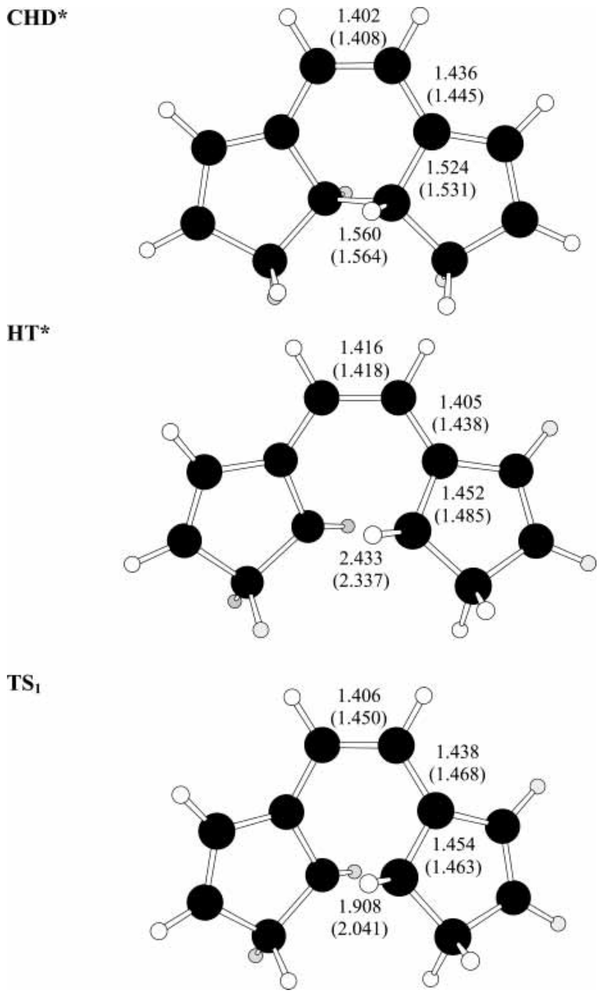

Figure 8. Optimized structures on the S_1 potential energy surface of system **4** at the CASSCF and MMVB levels. MMVB distances are in parentheses. Distances are in angstroms.

compared to the crossing, which looks like a much larger "hole" leading to the ground-state surface.

MMVB Force Field and Dynamics Simulation. The CASSCF results presented above explain part of the mechanism of diarylethene photochemistry, but a more detailed understanding requires dynamics. Unfortunately, a CASSCF dynamics study is beyond present computational resources for such large systems (Chart 1), and we have therefore used the MMVB method to generate the required energies and gradients. In this section, we first show that the hydrocarbon system **4** (Chart 1) is a reasonable model for systems **1**−**3** using CASSCF, and then we show that the MMVB and CASSCF results for **4** are comparable, before describing the results of the MMVB dynamics simulation for **4**. Our objective is to demonstrate that the nonadiabatic surface transition is feasible and to discover the geometries where "surface hops" occur. (The technical reasons for the choice of model system **4** are discussed in the Computational Methods section.) The determination of quantum yields is outside the scope of this work, as it would require more accurate potential surfaces than the present MMVB ones.

All of the stationary points located on the potential energy surfaces of systems **1**−**3** (Figures 4−6) have been found for system **4** using CASSCF (Figures 7−9), and the energy differences (Table 6) are all comparable (cf. Tables 1−5). We can therefore regard system **4** as a realistic model system for a theoretical study of the photochromism of diarylethenes **1**−**3**.

The same stationary points have also been located with MMVB. Figures 7−9 show that the MMVB and CASSCF geometries for **4** are in reasonable agreement: bond lengths are reproduced to within ~2%. The energetics are only qualitatively correct (compare Tables 6 and 7): for reasons discussed in the Computational Methods section, the closed-ring structures are all too low in energy relative to the open-ring structures. However, if we restrict ourselves to the open-ring side of the S_1 potential energy surface, MMVB is sufficient to investigate the dynamics of this system. Crucially, the conical intersection CI_3 is realistically described by MMVB: Figure 9 shows that both its geometry and the branching space (defined by the gradient difference and derivative coupling vectors) are essentially the same with CASSCF and MMVB. (Although the MMVB energy at CI_3 is too low compared to the case of HT*, it has no bearing on the mechanism, as the system hits the crossing seam at higher energies anyway, as discussed below.) In addition, minimum energy paths performed at the MMVB level starting from the Franck−Condon regions lead to the CHD* and HT* minima as in system **1**.

We now discuss the MMVB dynamics simulations (Tables 8 and 9). Following the strategy described in refs 35, 46, and 47 and summarized in the Computational Methods section, we have carried out semiclassical trajectory computations starting from two different regions of the S_1 potential energy surface. Analysis of the trajectories provides insight into the mechanism and approximate time scale of the photochromism of diaryl-

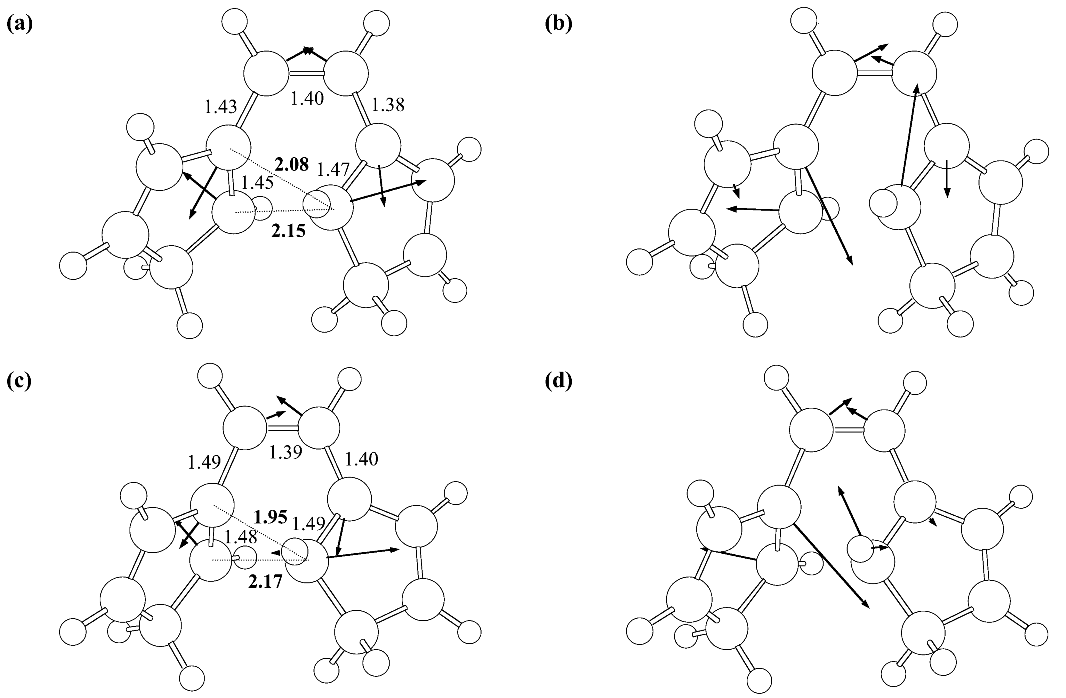

Figure 9. Optimized S_0/S_1 CI_3 in system **4** at the CASSCF and MMVB levels. (a) CASSCF derivative coupling vector, (b) CASSCF gradient difference vector, (c) MMVB derivative coupling vector, and (d) MMVB gradient difference vector. Distances are in angstroms.

TABLE 6: CASSCF(10,10)/4-31G Energies[a] for System 4 at Optimized Geometries

geometry	$\Delta E(S_1-S_0)$	$\Delta E(S_0)$	$\Delta E(S_1)$
HT	135.5	0.0	54.1
HT*	39.6	41.9	0.0
CI_1	0.7	100	22
CI_2	<0.1	111	30
CI_3	<0.1	100	21
CI_4	<0.1	114	33
CI_5	<0.1	123	42
CHD	116.5	−13.2	21.9
CHD*	65.3	7.8	−8.4
TS_0	40.7	43.3	2.5
TS_1	54.3	37.5	10.3

[a] Energies are in kilocalories per mole. Energies at conical intersection geometries are state-averaged. $\Delta E(S_0)$ and $\Delta E(S_1)$ are calculated with the open-ring S_0 and S_1 minimum energies, respectively, as references.

TABLE 7: MMVB Energies[a] for System 4 at Optimized Geometries

geometry	$\Delta E(S_1-S_0)$	$\Delta E(S_0)$	$\Delta E(S_1)$
HT	146.7	0.0	54.1
HT*	65.0	27.6	0.0
CI_1	<0.1	53.2	−39.4
CI_2	0.1	50.6	−41.9
CI_3	0.1	84.0	−8.5
CI_4	0.2	119.8	27.5
CI_5	0.8	121.0	29.2
CHD	131.3	−50.8	−12.1
CHD*	63.1	−24.9	−54.5
TS_0	83.2	18.4	9.0
TS_1	78.6	20.5	6.5

[a] Energies are in kilocalories per mole. $\Delta E(S_0)$ and $\Delta E(S_1)$ are calculated with the open-ring S_0 and S_1 minimum energies, respectively, as references.

ethenes. A total of 61 trajectories were computed: 41 starting from the HT FC region and 20 from the TS_1 region.

Table 8 shows that, of the trajectories started in the HT FC region, 23 reached the intermediate conical intersection CI_3, mostly within 2 ps. The isosceles triangular feature characterizing CI_3 is conserved (distance C_3C_9 is close to C_3C_8, in Table 8, cf. Chart 2), despite distortion due to the energy available from the FC region. Nine trajectories from HT FC hit different crossings (resembling CI_4 and CI_5) on the open-ring side close to the FC region. Finally, the nine remaining trajectories did not hit any crossing within the propagation time. None of the trajectories crossed the TS_1 barrier to give CHD*.

These results support the hypothesis that CI_3 is the critical structure at which rapid deactivation to the ground state occurs, before the system switches to the photoproduct. A closer analysis of the reactive trajectories provides a better understanding of the mechanism. Figures 10 and 11 present a typical reactive trajectory. The system reaches the HT* minimum region very quickly (Figure 10), that is, within a few femtoseconds (phase 1), due to the very steep gradient directed toward HT* on the S_1 potential energy surface at the Franck−Condon geometry. The resulting kinetic energy is redistributed in the large number of vibrational modes of the molecule, without finding the “exit” toward the excited closed-ring isomer formed by TS_1 (phase 2). Within a few picoseconds, the system encounters the CI_3 hyperline, as energy flows in one of the degeneracy-lifting coordinates (phase 3). Note the similarity of the “kink” at the conical intersection minimum (Figure 9) and the structure found for the $S_1 \rightarrow S_0$ radiationless decay (Figure 11). After decay to the ground state, the ring-closure takes place on S_0 and the system reaches the CHD photoproduct (phase 4).

The lifetime of the system in the HT* well ranges from ∼100 fs to several picoseconds, depending on the time taken for energy to flow into the necessary degeneracy-lifting coordinates. Although these lifetimes are approximate, they account for the competition observed between the fluorescence from HT* and the ring-closure reaction.[18] None of the trajectories we monitored passed through the transition state TS_1 to reach CHD*. This result seems surprising at first sight given the energy and time available: TS_1 lies only 6.5 kcal mol^{-1} above HT*, whereas the hopping event occurs at much higher energies, and we might initially expect the relative barrier heights to determine the rates.

TABLE 8: MMVB Dynamics Simulation for System 4: Results of the Trajectories Starting from HT[a]

trajectory	ΔE_{init}	ΔE_{hop}	S_1-S_0	C_3C_9	C_3C_8	C_8C_9	t_{hop}	t_{end}	CI type	product
reference		−8.5	0.1	2.17	1.95	1.48			CI_3	
1	58.1	30.2	6.7	2.34	2.02	1.60	766.9	3682	CI_3	HT
2	56.2	30.5	2.5	2.24	1.99	1.51	1927.8	4007	CI_3	CHD
3	63.2	30.7	4.9	2.33	2.03	1.59	2788.4	4522	CI_3	HT
4	62.8	34.7	3.9	2.41	2.14	1.57	963.3	3495	CI_3	CHD
5	57.9	34.8	1.3	2.34	2.06	1.54	232.8	3824	CI_3	HT
6	56.6	36.3	3.4	2.32	2.07	1.49	3985.1	5167	CI_3	HT
7	63.2	38.4	5.1	2.39	2.05	1.53	1373.0	2546	CI_3	CHD
8	59.4	40.9	8.6	2.46	2.04	1.53	757.2	783	CI_3	indeterminate
9	70.1	41.9	6.1	2.35	1.99	1.53	3609.6	6222	CI_3	HT
10	61.6	49.1	4.2	2.32	2.07	1.53	4666.6	5702	CI_3	HT
11	62.2	50.4	5.5	2.13	2.03	1.48	1981.7	5406	CI_3	CHD
12	61.3	50.4	6.0	2.29	2.08	1.48	2090.8	2114	CI_3	indeterminate
13	54.8	62.3	3.6	2.30	1.99	1.44	3443.6	3466	CI_3	indeterminate
14	63.2	62.3	6.2	2.20	2.23	1.46	187.6	3221	CI_3	HT
15	66.6	65.7	4.4	2.71	2.23	1.54	139.7	4748	CI_3	HT
16	67.0	67.7	5.9	2.70	2.28	1.59	824.3	3480	CI_3	HT
17	77.4	68.7	5.7	2.26	2.00	1.43	299.2	337	CI_3	indeterminate
18	62.9	70.8	5.4	2.49	2.12	1.59	667.7	4984	CI_3	HT
19	69.4	71.8	2.1	2.51	2.01	1.63	1123.3	3331	CI_3	HT
20	54.6	72.2	5.9	2.39	2.21	1.53	1895.8	3664	CI_3	HT
21	52.3	73.5	2.2	2.27	2.07	1.48	207.3	3206	CI_3	HT
22	55.6	88.5	6.1	5.54	4.46	1.58	1247.1	3176	CI_5	HT
23	54.6	93.8	6.8	2.31	2.06	1.45	1277.0	1299	CI_3	indeterminate
24	61.3	120.5	4.0	4.97	4.25	1.57	4707.5	4871	CI_5	HT
25	62.6	121.3	4.6	2.52	2.21	1.59	1194.6	2985	CI_3	HT
26	61.4	143.1	6.7	5.75	4.83	1.60	1196.0	1241	CI_5	indeterminate
27	58.5	154.8	2.9	5.20	4.11	1.54	286.2	2397	CI_4	indeterminate
28	61.8	155.9	5.1	3.51	4.02	1.69	233.5	669	CI_4	indeterminate
29	57.4	178.2	11.6	3.14	3.90	1.39	122.9	134	CI_5	indeterminate
30	70.8	186.4	5.4	3.80	4.21	1.59	222.0	356	CI_4	HT
31	56.5	241.1	6.7	4.45	3.65	1.50	217.3	230	CI_5	indeterminate
32	77.3	243.4	6.7	3.80	3.95	1.81	197.8	271	CI_4	indeterminate
33	65.8						no hop	5844		
34	64.8						no hop	5044		
35	64.9						no hop	6069		
36	58.8						no hop	5974		
37	63.4						no hop	5387		
38	75.1						no hop	7346		
39	67.0						no hop	6415		
40	58.1						no hop	6020		
41	68.2						no hop	5817		

[a] Data for the optimized CI_3 structure are given as a reference. ΔE values are calculated with the open-ring S_1 minimum energy as reference. ΔE_{init} refers to the initial potential energy difference, whereas ΔE_{hop} refers to the energy difference at the hop. Energies are in kilocalories per mole, distances are in angstroms, and time is in femtoseconds. Carbon atoms are numbered as Figure 2.

However, this is not comparing like with like. As shown in Figure 3, the CI_3 crossing seam lies in the vicinity of the HT* well and extends over a wide range of geometries as the electronic degeneracy is preserved in a $3N - 8$ dimensional subspace of the internuclear coordinates. Therefore, the probability for the system to go through the TS_1 "bottleneck" is very small compared to that of hitting the crossing hyperline, as the partially equilibrated fluctuations taking place in the HT* well are far more likely to bring the system to the crossing seam than across the energy barrier. This is illustrated in Figure 11, where the fluctuations occurring in the HT* region on the S_1 potential energy surface are clearly visible before a particular vibrational mode brings the system to the CI_3 crossing seam.

In addition, Table 8 shows that the system hits the CI_3 crossing seam over a large energy range of ~90 kcal mol^{-1}, ranging from 30.2 to 121.3 kcal mol^{-1} above the HT* minimum energy. (A similar phenomenon has previously been encountered in a study of the dihydroazulene/vinylheptafulvene photochromic couple.[54]) The mechanism we propose above explains this and also accounts for the absence of appreciable temperature dependence for the ring-closure.[17] Because the real activation energies are certainly lower than the ones calculated, and also because of vibrational deactivation by the solvent not simulated here, we expect the higher energy trajectories to be unrealistic. The important point is that since there is so much excess energy already, the rate-limiting step is waiting for sufficient energy to randomly enter a coordinate orthogonal to the initial reaction path that leads to the crossing.

Twenty trajectories starting from the TS_1 region were propagated for up to ~4 ps, simulating the ring-opening process (Table 9). Of these trajectories, 14 hit the crossing seam, most of them within 2 ps. The geometry at the hop identifies the seam as CI_3 in this case too (Scheme 2 and Figure 3). The quantum yield is relatively low for ring-opening compared to ring-closure in general. This may be due to the fact that the system has to first go through the "bottleneck" formed by TS_1 before reaching CI_3, allowing time for fluorescence to take place.[19] Another reason could be access to the $CI_{1,2}$ funnels as the system spends time vibrating in the CHD* well. This second hypothesis seems more likely, as no evidence of stronger fluorescence from CHD* relative to HT* has been observed. The ring-opening activated process accounts as well for the temperature dependence observed in the quantum yield.[17] Indeed, the ring-opening quantum yield increases with temperature as the system has more available energy to overcome the barrier.

TABLE 9: MMVB Dynamics Simulation for System 4: Results of the Trajectories Starting from TS_1[a]

trajectory	ΔE_{init}	ΔE_{hop}	S_1-S_0	C_3C_9	C_3C_8	C_8C_9	t_{hop}	t_{end}	CI type	product
reference		−8.5	0.1	2.17	1.95	1.48			CI_3	
1	28.6	9.9	4.9	2.27	2.03	1.55	1488.9	2576	CI_3	CHD
2	28.1	10.8	5.3	2.28	2.03	1.51	2384.6	3078	CI_3	CHD
3	26.5	11.2	0.1	2.25	2.00	1.42	1314.6	2516	CI_3	CHD
4	27.3	13.8	2.9	2.20	2.04	1.54	3569.9	3751	CI_3	CHD
5	28.3	14.7	4.7	2.31	2.06	1.50	2777.7	2905	CI_3	HT
6	26.9	15.2	5.3	2.23	2.00	1.50	2517.9	2560	CI_3	indeterminate
7	23.3	15.8	7.2	2.24	2.03	1.49	2216.4	2327	CI_3	HT
8	27.5	16.7	4.5	2.33	2.05	1.54	1542.8	2106	CI_3	HT
9	40.6	16.8	10.6	2.21	1.99	1.48	2166.9	2914	CI_3	HT
10	30.4	18.5	3.9	2.35	2.12	1.57	3076.5	3214	CI_3	HT
11	20.8	19.1	4.2	2.18	1.96	1.47	3803.2	4041	CI_3	HT
12	34.9	21.8	5.2	2.27	2.04	1.46	2662.0	2773	CI_3	HT
13	39.1	22.9	3.8	2.29	1.99	1.57	1472.7	1493	CI_3	indeterminate
14	26.2	23.4	3.7	2.25	2.00	1.53	1450.1	2605	CI_3	CHD
15	26.9						no hop	3991		
16	20.8						no hop	4272		
17	22.4						no hop	4215		
18	30.1						no hop	3797		
19	21.1						no hop	4235		
20	26.8						no hop	3943		

[a] Data for the optimized CI_3 structure are given as a reference. ΔE values are calculated with the open-ring S_1 minimum energy as reference. ΔE_{init} refers to the initial potential energy difference, whereas ΔE_{hop} refers to the energy difference at the hop. Energies are in kilocalories per mole, distances are in angstroms, and time is in femtoseconds.

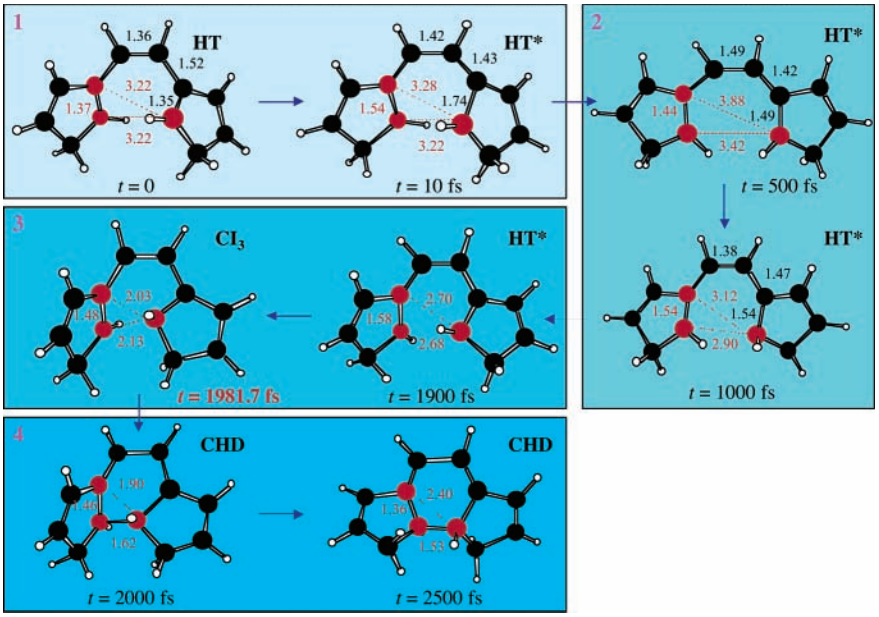

Figure 10. Description of the four phases in a typical MMVB trajectory started on the HT side: (1) ultrafast relaxation to HT*; (2) motion on S_1 in the HT* minimum well; (3) energy flowing in one of the degeneracy-lifting coordinates and the system decaying at CI_3; and (4) ring-closure on the ground state.

Conclusions

An ab initio molecular orbital study of three different diarylethene derivatives and a prototype hydrocarbon model system is presented. The origin of the photochromic properties of these systems is a conical intersection (which we have located computationally), but the key result of this work is that dynamics are necessary to explain why the conical intersection is accessible. The reason is that the excited-state reaction path is not contained in the branching space defining the intersection, which is quite different from the case of other prototypical fast reactions from excited states, for example, azulene, where the initial relaxation is strongly directed toward the crossing.[45]

MMVB dynamics calculations were carried out on a hydrocarbon model system, which preserves the topological features of the diarylethene PESs, to support our interpretation of the mechanism of the photochemical process investigated. Both ring-closure and ring-opening have been rationalized on the basis of the topological features of the S_0 and S_1 potential energy surfaces, the analysis of the reaction path relative to the branching space, and the dynamics calculations. Figures 3 and 12 summarize the results obtained.

For the ring-closure reaction, the system decays to S_0 at the crossing CI_3 before finding the “bottleneck” formed by the transition structure TS_1 on S_1. This is due to the fact that the crossing hyperline extends over a wide range of nuclear configurations and the probability for the system to go through the transition state TS_1 is therefore small compared to that of hitting the crossing seam CI_3. Moreover, since the reaction path is parallel to the crossing seam, the system can encounter it over a wide range of energies. At the crossing, efficient decay

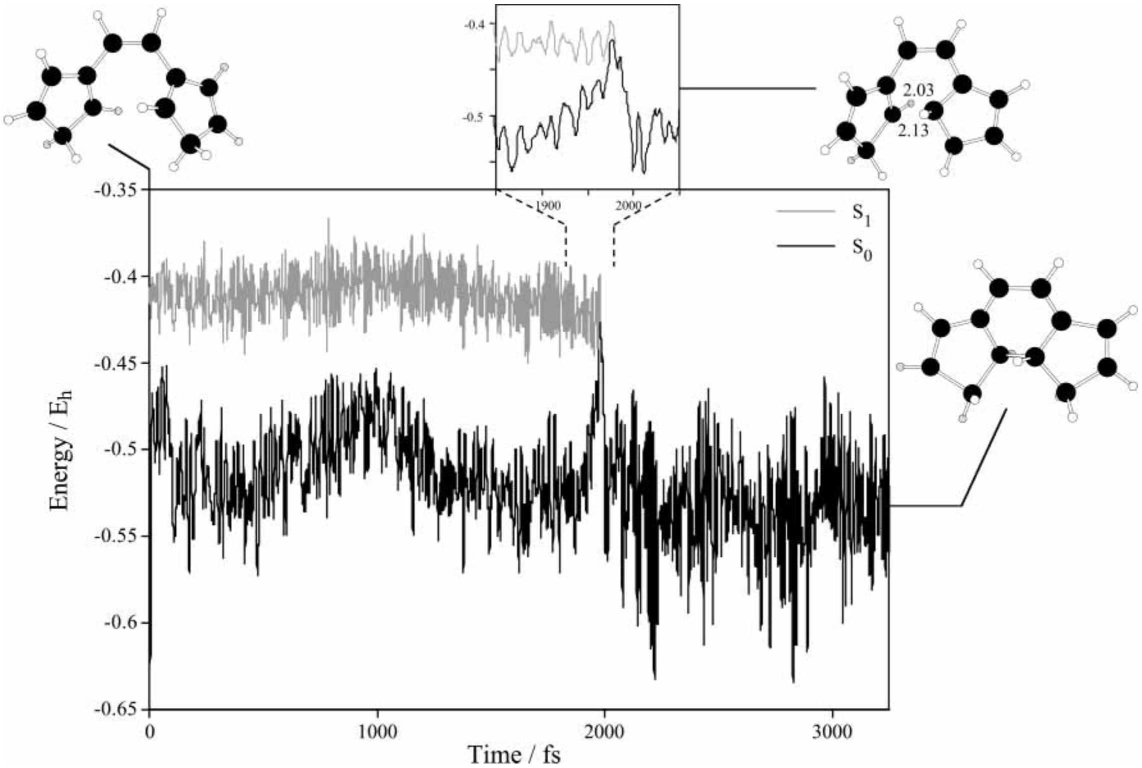

Figure 11. Typical MMVB trajectory started on the HT side with random sampling from a ground-state trajectory calculation. The starting geometry is shown at the top left, the one at which the $S_1 \rightarrow S_0$ surface hop takes place at the top right, and the final photoproduct at the bottom right. The inset displays a magnified view of the electronic energies near the hop.

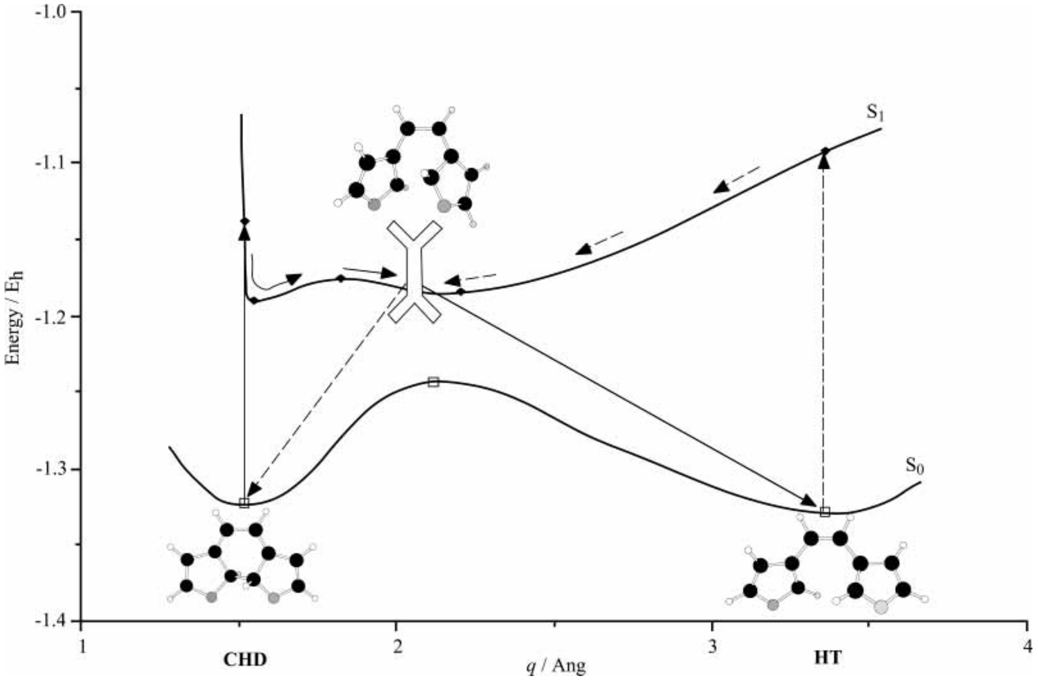

Figure 12. Outline of the two reaction paths corresponding to the ring-opening (plain arrows) and ring-closure (dashed arrows) of diarylethenes.

to the ground state potential energy surface takes place, leading subsequently to the CHD minimum. This mechanism accounts for the highly effective and ultrafast ring-closure.

On the other hand, the ring-opening reaction encounters a potential energy barrier on S_1, before reaching the same relaxation funnel that is involved in the ring-closure. Then, fast deactivation to the ground state takes place and leads to the formation of HT. The existence of a potential energy barrier along the pathway accounts for the temperature dependence and the relatively low quantum yield observed. Moreover, several conical intersections near CHD* provide photophysical decay pathways back to CHD**,** decreasing the ring-opening quantum yield. We cannot predict whether these funnels are more accessible than those lying on the HT side, as the MMVB potential proved unreliable for CHD structures. Hence, we cannot say anything definitive about the relative fluorescence yields from CHD* and HT*.

The type of surface topology documented in this work merits study as a test system for coherent control in ultrafast photochemical reactions.[55] Shaped laser excitation pulses to guide the chemical reaction from initial to final states could be used to enhance the efficiency of nonadiabatic transitions. A sequence of laser pulses could be designed in such a way that the wave packet is driven systematically to the CI_3 crossing seam to enhance the ring-closure rate. Similarly, the system could be directed toward the transition state to increase the ring-opening quantum yield.

Acknowledgment. This research was supported by the European Union. We thank Professor Masahiro Irie for suggesting this problem. All calculations were run on an IBM SP2, using development versions of the *Gaussian 99* program.

Supporting Information Available: Figures S1−S5 showing the optimized structures found for systems **2** and **3**. Figure S6 giving an illustration of the reaction paths arising from CI_3. Figure S7 providing the results for other S_0/S_1 conical intersections of system **1**. Tables 1−7 listing energies for the optimized geometries of systems **1**−**4**. Table of Cartesian coordinates of optimized CASSCF structures of system **1**. This material is available free of charge via the Internet at http://pubs.acs.org.

References and Notes

(1) Irie, M. *Chem. Rev.* **2000**, *100*, 1683.

(2) Bouas-Laurent, H.; Dürr, H. *Pure Appl. Chem.* **2001**, *73*, 639−665.

(3) Berkovic, G.; Krongauz, V.; Weiss, V. *Chem. Rev.* **2000**, *100*, 1741−1753.

(4) Yokoyama, Y. *Chem. Rev.* **2000**, *100*, 1717−1739.

(5) Irie, M. *Chem. Rev.* **2000**, *100*, 1685−1716.

(6) Tamai, N.; Miyasaka, H. *Chem. Rev.* **2000**, *100*, 1875−1890.

(7) Tamai, N.; Sakai, T.; Shimidzu, T.; Irie, M. *J. Phys. Chem.* **1996**, *100*, 4689−4692.

(8) Ern, J.; Bens, A. T.; Bock, A.; Martin, H.-D.; Kryschi, C. *J. Lumin.* **1998**, *76*, 90−94.

(9) Ern, J.; Bens, A. T.; Martin, H.-D.; Mukamel, S.; Schmid, D.; Tretiak, S.; Tsiper, E.; Kryschi, C. *Chem. Phys.* **1999**, *246*, 115−125.

(10) Ern, J.; Bens, A. T.; Martin, H.-D.; Mukamel, S.; Schmid, D.; Tretiak, S.; Tsiper, E.; Kryschi, C. *J. Lumin.* **2000**, *87*, 742−744.

(11) Miyasaka, H.; Nobuto, T.; Itaya, A.; Tamai, N.; Irie, M. *Chem. Phys. Lett.* **1997**, *269*, 281−285.

(12) Owrutsky, J. C.; Nelson, H. H.; Baronavski, A. P.; Kim, O.-K.; Tsivgoulis, G. M.; Gilat, S. L.; Lehn, J.-M. *Chem. Phys. Lett.* **1998**, *293*, 555−563.

(13) Hania, P. R.; Telesca, R.; Lucas, L. N.; Pugzlys, A.; van Esch, J.; Feringa, B. L.; Snijders, J. G.; Duppen, K. *J. Phys. Chem. A* **2002**, *106*, 8498−8507.

(14) Shibata, K.; Muto, K.; Kobatake, S.; Irie, M. *J. Phys. Chem. A* **2002**, *106*, 209−214.

(15) Miyasaka, H.; Murakami, M.; Itaya, A.; Guillaumont, D.; Nakamura, S.; Irie, M. *J. Am. Chem. Soc.* **2001**, *123*, 753−754.

(16) Miyasaka, H.; Murakami, M.; Okada, T.; Nagata, Y.; Itaya, A.; Kobatake, S.; Irie, M. *Chem. Phys. Lett.* **2003**, *371*, 40−48.

(17) Irie, M.; Lifka, T.; Kobatake, S.; Kato, N. *J. Am. Chem. Soc.* **2000**, *122*, 4871−4876.

(18) Tanaka, N.; Okabe, C.; Sakota, K.; Fukaminato, T.; Kawai, T.; Irie, M.; Goldberg, A.; Nakamura, S.; Sekiya, H. *THEOCHEM* **2002**, *616*, 113−118.

(19) Kim, M.-S.; Kawai, T.; Irie, M. *Opt. Mater.* **2002**, *21*, 271−274. (b) Kawai, T.; Kim, M.-S.; Sasaki, T.; Irie, M. *Opt. Mater.* **2002**, *21*, 275−278.

(20) Cho, H.-G.; Cheong, B.-S. *Bull. Korean Chem. Soc.* **1998**, *19*, 308−313.

(21) Majumdar, D.; Lee, H. M.; Kim, J.; Kim, K. S.; Mhin, B. J. *J. Chem. Phys.* **1999**, *111*, 5866−5872.

(22) Uchida, K.; Guillaumont, D.; Tsuchida, E.; Mochizuki, G.; Irie, M.; Murakami, A.; Nakamura, S. *THEOCHEM* **2002**, *579*, 115−120.

(23) Guillaumont, D.; Kobayashi, T.; Kanda, K.; Miyasaka, H.; Ushida, K.; Kobatake, S.; Shibata, K.; Nakamura, S.; Irie, M. *J. Phys. Chem. A* **2002**, *106*, 7222−7227.

(24) Halász, G.; Vibók, Á.; Mebel, A. M.; Baer, M. *J. Chem. Phys.* **2003**, *118*, 3052−3064 and references therein.

(25) Celani, P.; Garavelli, M.; Ottani, S.; Bernardi, F.; Robb, M. A.; Olivucci, M. *J. Am. Chem. Soc.* **1995**, *117*, 11584−11585.

(26) Bernardi, F.; Olivucci, M.; Robb, M. A. *Isr. J. Chem.* **1993**, *33*, 265−276.

(27) Garavelli, M.; Smith, B. R.; Bearpark, M. J.; Bernardi, F.; Olivucci, M.; Robb, M. A. *J. Am. Chem. Soc.* **2000**, *122*, 5568−5581.

(28) Olivucci, M.; Bernardi, F.; Celani, P.; Ragazos, I.; Robb, M. A. *J. Am. Chem. Soc.* **1994**, *116*, 1077−1085.

(29) Celani, P.; Ottani, S.; Olivucci, M.; Bernardi, F.; Robb, M. A. *J. Am. Chem. Soc.* **1994**, *116*, 10141−10151.

(30) Celani, P.; Bernardi, F.; Robb, M. A.; Olivucci, M. *J. Phys. Chem.* **1996**, *100*, 19364−19366.

(31) Garavelli, M.; Celani, P.; Fato, M.; Bearpark, M. J.; Smith, B. R.; Olivucci, M.; Robb, M. A. *J. Phys. Chem. A* **1997**, *101*, 2023−2032.

(32) Garavelli, M.; Page, C. S.; Celani, P.; Olivucci, M.; Schmid, W. E.; Trushin, S. A.; Fuss, W. *J. Phys. Chem. A* **2001**, *105*, 4458−4469.

(33) For example: Salem L. *Electrons in Chemical Reactions: First Principles*; Wiley: New York, 1982; p 151.

(34) Atchity, G. J.; Xantheas, S. S.; Ruedenberg, K. *J. Chem. Phys.* **1991**, *95*, 1862−1876.

(35) Bearpark, M. J.; Robb, M. A.; Smith, B. R.; Bernardi, F.; Olivucci, M. *Chem. Phys. Lett.* **1995**, *242*, 27−32.

(36) Hehre, W. J.; Stewart, R. F.; Pople, J. A. *J. Chem. Phys.* **1969**, *51*, 2657−2664. (b) Hehre, W. J.; Ditchfield, R.; Stewart, R. F.; Pople, J. A. *J. Chem. Phys.* **1970**, *52*, 2769−2773. (c) Ditchfield, R.; Hehre, W. J.; Pople, J. A. *J. Chem. Phys.* **1971**, *54*, 724−728. (d) Hehre, W. J.; Ditchfield, R.; Pople, J. A. *J. Chem. Phys.* **1972**, *56*, 2257−2261. (e) Hariharan, P. C.; Pople, J. A. *Theor. Chim. Acta* **1973**, *28*, 213−222. (f) Hariharan, P. C.; Pople, J. A. *Mol. Phys.* **1974**, *27*, 209. (g) Gordon, M. S. *Chem. Phys. Lett.* **1980**, *76*, 163−168. (h) Petersson, G. A.; Bennett, A.; Tensfeldt, T. G.; Al-Laham, M. A.; Shirley, W. A.; Mantzaris, J. *J. Chem. Phys.* **1988**, *89*, 2193−2218.

(37) Frisch, M. J.; Trucks, G. W.; Schlegel, H. B.; Scuseria, G. E.; Robb, M. A.; Cheeseman, J. R.; Zakrzewski, V. G.; Montgomery, J. A., Jr.; Stratmann, R. E.; Burant, J. C.; Dapprich, S.; Millam, J. M.; Daniels, A. D.; Kudin, K. N.; Strain, M. C.; Farkas, O.; Tomasi, J.; Barone, V.; Cossi, M.; Cammi, R.; Mennucci, B.; Pomelli, C.; Adamo, C.; Clifford, S.; Ochterski, J.; Petersson, G. A.; Ayala, P. Y.; Cui, Q.; Morokuma, K.; Malick, D. K.; Rabuck, A. D.; Raghavachari, K.; Foresman, J. B.; Ortiz, J. V.; Baboul, A. G.; Cioslowski, J.; Stefanov, B. B.; Liu, G.; Liashenko, A.; Piskorz, P.; Komaromi, I.; Gomperts, R.; Martin, R. L.; Fox, D. J.; Keith, T.; Al-Laham, M. A.; Peng, C. Y.; Nanayakkara, A.; Gonzalez, C.; Challacombe, M.; Gill, P. M. W.; Johnson, B.; Chen, W.; Wong, M. W.; Andres, J. L.; Gonzalez, C.; Head-Gordon, M.; Replogle, E. S.; Pople, J. A. *Gaussian 99*, Development Version, revision B.06; Gaussian, Inc.: Pittsburgh, PA, 1998.

(38) Ragazos, I. N.; Robb, M. A.; Bernardi, F.; Olivucci, M. *Chem. Phys. Lett.* **1992**, *197*, 217−223. (b) Bearpark, M. J.; Robb, M. A.; Schlegel, H. B. *Chem. Phys. Lett.* **1994**, *223*, 269−274.

(39) Yamamoto, N.; Vreven, T.; Robb, M. A.; Frisch, M. J.; Schlegel, H. B. *Chem. Phys. Lett.* **1996**, *250*, 373−378.

(40) Celani, P.; Robb, M. A.; Garavelli, M.; Bernardi, F.; Olivucci, M. *Chem. Phys. Lett.* **1995**, *243*, 1−8.

(41) Bernardi, F.; Olivucci, M.; Robb, M. A. *J. Am. Chem. Soc.* **1992**, *114*, 1606−1616.

(42) Allinger, N. L. *Adv. Phys. Org. Chem.* **1976**, *13*, 1−85.

(43) Anderson, P. W. *Phys. Rev.* **1959**, *115*, 2−13. (b) Said, M.; Maynau, D.; Malrieu, J.-P.; Bach, M.-A. G. *J. Am. Chem. Soc.* **1984**, *106*, 571−579. (c) Said, M.; Maynau, D.; Malrieu, J.-P. *J. Am. Chem. Soc.* **1984**, *106*, 580−587. (d) Durand, P.; Malrieu, J.-P. *Adv. Chem. Phys.* **1987**, *67*, 321−412.

(44) Bearpark, M. J.; Bernardi, F.; Olivucci, M.; Robb, M. A. *Chem. Phys. Lett.* **1994**, *217*, 513−519.

(45) Bearpark, M. J.; Bernardi, F.; Clifford, S.; Olivucci, M.; Robb, M. A.; Smith, B. R.; Vreven, T. *J. Am. Chem. Soc.* **1996**, *118*, 169−175.

(46) Preston, R. K.; Tully, J. C. *J. Chem. Phys.* **1971**, *54*, 4297. (b) Preston, R. K.; Tully, J. C. *J. Chem. Phys.* **1971**, *55*, 562−572.

(47) Helgaker, T.; Uggerud, E.; Jensen, H. J. A. *Chem. Phys. Lett.* **1990**, *173*, 145−150.

(48) Boggio-Pasqua, M.; Bearpark, M. J.; Klene, M.; Robb, M. A. In preparation, and references therein.

(49) Hayden, C. C.; Chandler, D. *J. Phys. Chem.* **1995**, *99*, 7897−7903. (b) Fuss, W.; Schikarski, T.; Schmid, W. E.; Trushin, S. A.; Hering, P.; Kompa, K. L. *J. Chem. Phys.* **1997**, *106*, 2205−2211. (c) Garavelli, M.; Celani, P.; Bernardi, F.; Robb, M. A.; Olivucci, M. *J. Am. Chem. Soc.* **1997**, *119*, 11487−11494.

(50) Fuss, W.; Schmid, W. E.; Trushin, S. A. *J. Chem. Phys.* **2000**, *112*, 8347−8362.

(51) Serrano-Andres, L.; Lindh, R.; Roos, B. O.; Merchan, M. *J. Phys. Chem.* **1993**, *97*, 9360−9368.

(52) Nakayama, K.; Nakano, H.; Hirao, K. *Int. J. Quantum Chem.* **1998**, *66*, 157−175.

(53) Nakamura, S.; Irie, M. *J. Org. Chem.* **1988**, *53*, 6136−6138.

(54) Boggio-Pasqua, M.; Bearpark, M. J.; Hunt, P. A.; Robb, M. A. *J. Am. Chem. Soc.* **2002**, *124*, 1456−1470.

(55) de Vivie-Riedle, R.; Kurtz, L.; Hofmann, A. *Pure Appl. Chem.* **2001**, *73*, 525−528.